

Energy-band-structure study of the (100), (110), and (111) surfaces of TiC

A. Callenås and L. I. Johansson

Department of Physics and Measurement Technology, Linköping University, S-581 83 Linköping, Sweden

A. N. Christensen

Department of Chemistry, Aarhus University, DK-8000 Aarhus C, Denmark

K. Schwarz and J. Redinger

Institute of Technical Electrochemistry, Technical University of Vienna, Getreidemarkt 9, A-1060 Vienna, Austria

(Received 13 September 1982)

The band structure of a $\text{TiC}_{0.93}$ crystal has been studied by angle-resolved photoemission. Experiments were carried out on the (100), (110), and (111) surfaces. The bulk band structure of $\text{TiC}_{1.0}$ has been calculated using the linear augmented-plane-wave method, and the results are used to interpret the experimental data. The results indicate that most of the structures observed in the photoemission spectra from the (100) surface can be explained in terms of direct transitions.

I. INTRODUCTION

Interest in the exceptional bonding properties of transition-metal carbides and nitrides has stimulated a number of studies of their electronic structure in recent years.¹⁻¹⁸ Most of the experimental studies to date have provided information about the total density of occupied states and have thus not been very sensitive to details of the band structure. In some recent investigations, however, where the angle-resolved photoemission spectroscopy (ARPES) technique was utilized, information about band dispersions, critical-point energies, and surface electronic states have been obtained for TiC (Ref. 14) and TiN (Ref. 15) surfaces. These results allowed direct detailed comparisons to calculated band structures. The primary aim with the present study is a comparison of experimental (ARPES) and calculated [linearized augmented-plane-wave method (LAPW)] results of the bulk band structure of TiC.

Since the conclusions drawn in the previous ARPES studies of the bulk band structure of TiC and TiN differ somewhat, it is also worthwhile to try to clarify and pinpoint the discrepancies. In the study¹⁴ of the (100) and (111) surfaces of a $\text{TiC}_{0.93}$ crystal the identification and mapping of the dispersion of individual bands were found to be difficult because three-dimensional density-of-states features were observed in normal emission spectra at most photon energies. These features were attributed to either the effects of bulk vacancies in the crystal or to surface inhomogeneities incurred in the preparation process. In the study¹⁵ of the (100) surface of a

$\text{TiN}_{0.83}$ crystal, on the other hand, direct transitions were shown to make a dominant contribution to the photoemission spectrum, i.e., individual bands and their dispersions were mapped out by assuming direct transitions. Another experimental investigation of TiC therefore seemed necessary to us, especially when combined with a band-structure calculation carried out to high enough final-state energies to allow a direct comparison. In this study we report the results of a LAPW band-structure calculation for the stoichiometric composition $\text{TiC}_{1.0}$, carried out to final-state energies of about 40 eV above the Fermi level. These calculated results are used in the analysis of the ARPES results.

II. EXPERIMENTAL

Angle-resolved photoemission measurements have been performed using resonance radiation from a differentially pumped uv lamp (He I and Ne I radiation; 21.2 and 16.85 eV, respectively). The emitted electrons were energy analyzed with a movable hemispherical electrostatic analyzer, having an acceptance "cone" represented by a rectangle of dimensions $\pm 1^\circ$ by $\pm 3^\circ$. The energy resolution of the energy analyzer was about 0.2 eV. The spectrometer had a base pressure of less than 1×10^{-10} Torr.

Single crystals of $\text{TiC}_{0.93}$ were made using a vertical floating-zone technique.¹⁹ The TiC(100) and the TiC(110) crystals were cleaned *in situ* by high-temperature flashings. Flashings to about 1500°C were found to produce clean surfaces. In order to get a clean TiC(111) surface we found it necessary

also to do some Ar^+ -ion sputtering to get rid of the residual oxygen. To maintain a clean TiC(111) surface during measurement, high-temperature flashings about once an hour were necessary. The (100) and (110) surfaces, on the other hand, stayed clean for several hours. The cleanliness of the samples was checked with Auger electron spectroscopy. In Fig. 1 the Auger spectrum for a TiC(111) crystal sputtered and (to 1500°C) annealed is shown. There is no sign in the spectrum of residual oxygen or other contaminating elements. In contrast to the measurements done by Weaver *et al.*¹⁴ we did not observe any change of the [Ti]/[C] ratio as the annealing temperature was increased from 1000 to 1600°C. The [Ti]/[C] ratio was, however, reduced somewhat after sputtering and annealing cycles. The $[\text{Ti}]_{418\text{ eV}}/[\text{C}]_{273\text{ eV}}$ ratio observed was 0.96 before and 0.87 after sputtering and annealing. We have compared the $[\text{Ti}]_{418\text{ eV}}$ peak and the $[\text{C}]_{273\text{ eV}}$ peak, since these peaks can be used for quantitative analysis without any corrections for peak shape changes with concentration. The shape of the $[\text{Ti}]_{387\text{ eV}}$ peak has been reported²⁰ to change with concentration.

The crystals were oriented azimuthally prior to mounting in the spectrometer with the aid of x-ray diffraction and the channeling patterns observed in a scanning electron microscope. In the spectra shown below, the incidence angle of the radiation θ_i and the electron emission angle θ_e are given relative to the sample surface normal. The midpoint of the Fermi edge is used as the reference level for all spectra.

III. RESULTS AND DISCUSSION

A. Band-structure calculation

An energy band-structure calculation which properly includes the effects of exchange and correlation

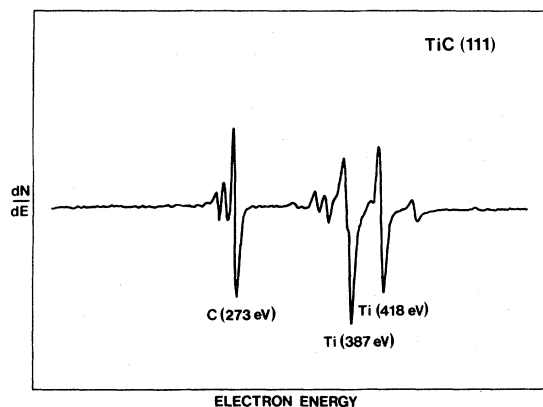


FIG. 1. Auger electron spectrum of a sputtered and annealed, to 1500°C, TiC(111) crystal.

describes the elementary excitations of the solid system.²¹ Density-functional theory²² (DFT) is used to introduce these effects in a simple but efficient manner. Within DFT the resulting eigenvalues $\epsilon(k,n)$ are not rigorously the system excitation (quasiparticles) energies, except at the Fermi level.²³ In practical applications, however, they appear to be a good approximation in extended systems, but experiments exhibit larger deviations in narrow $3d$ bands of transition metals or valence bands of insulators. But a great deal of these discrepancies has to be attributed to some shortcomings in the commonly used local density-functional (LDF) approximations to DFT, such as $X\alpha$ (Ref. 24) or other more sophisticated prescriptions of how to construct the local exchange-correlation potential.²⁵ For metals like Rh and Ni or semiconductors like Si, some recent publications have shown that LDF band energies can be improved by 0.2–0.9 eV with respect to experiment by either employing nonlocal corrections to LDF (Ref. 26) or—in order to account for excited states effects—by including a complex self-energy²⁷ in the quasiparticle Green's function. Considering problems such as, e.g., different stoichiometry in the real crystal and the calculated crystal, it was not justified to undertake these rather tedious corrections to the LDF eigenvalues.

By keeping these general remarks in mind we use for the present analysis just the LDF energy bands of $\text{TiC}_{1.0}$ up to 40 eV above the Fermi level. Since none of the available band structures exist up to high enough energies and on a fine enough \vec{k} grid, we performed new calculations based on the self-consistent $X\alpha$ crystal potential given by Neckel *et al.*²⁸ The energies were calculated for a plane through the Brillouin zone surrounded by the \vec{k} points $\Gamma-(\Delta)-X-U-L-K-(\Sigma)-\Gamma$. In this plane a uniform mesh of 149 \vec{k} points is obtained by dividing the Δ direction into 16 and the Σ direction into 12 intervals.

The actual computation was done in two steps: First, we used the fully symmetrized APW method²⁸ to extend the band structure up to the desired energies for high-symmetry \vec{k} points. In the second step the significantly faster LAPW method²⁹ was employed to obtain the band energies for all \vec{k} points of the chosen grid with the augmented-plane-wave (APW) eigenvalues serving as a check for the accuracy of the linearization scheme, which is known to be adequate over an energy range of about 1 Ry. Five energy regions were required to span the whole energy range of interest. The parameters E_l (for definition see Ref. 29) for the radial wave functions inside the atomic spheres are given in Table I. This choice of parameters gives an agreement of the band energies between the LAPW and APW method to

TABLE I. Energy parameters for the LAPW calculations: E_{sep} separates the different energy regions; E_l^t is the energy around which the l -like radial wave function inside atomic sphere t is expanded. All energies are given with respect to the muffin-tin zero (E_F is at 0.664 Ry) and in Ry.

Region	E_{sep}	
1		C sphere: $E_l=0.4$ Ry except $E_s^C=-0.2$ Ry Ti sphere: $E_l=0.7$ Ry except $E_p^{\text{Ti}}=0.0$ Ry
	0.9 Ry	
2		All $E_l=1.0$ Ry
	1.3 Ry	
3		All $E_l=1.6$ Ry
	2.0 Ry	
4		All $E_l=2.4$ Ry
	2.8 Ry	
5		All $E_l=3.2$ Ry

within a few mRy. By combining the LAPW eigenvalues from the five energy sheets and by using the symmetrized APW results together with the compatibility relations we obtained the complete band structure shown in Fig. 2. Also shown in Fig. 2 is a free-electron final-state band (dotted line).

It should be pointed out that the LDF results locate the lowest occupied band, the C 2s band, about 1 eV closer to the Fermi level than the experimental

results.¹⁴ This difference may be due to the assumptions concerning the exchange-correlation potential as discussed recently.³⁰

B. The (100) surface

Angle-resolved electron energy distribution curves (EDC's) recorded from the TiC(100) surface using a photon energy of 21.2 eV are shown in Fig. 3. The EDC's are recorded at different polar angles θ_e , along the $\langle 011 \rangle$ azimuth. The spectra are normalized to a constant peak height of the dominant structure. For the spectra shown in Fig. 3(a), the incidence angle θ_i is 45° while it is 15° for those shown in Fig. 3(b). For the normal emission spectrum, $\theta_e=0^\circ$, in Fig. 3(a) there are indications of five emission peaks. There are two peaks close to the Fermi level (within 2 eV), two peaks between -2.5 and -4 eV, and one peak at about -6 eV.

A strong polarization effect is observed when comparing Figs. 3(a) and 3(b). From the observed polarization dependence the symmetry of the initial state can directly be identified. For normal electron emission, symmetry selection rules³¹ give that $E_{||}$, i.e., the component of the electric field parallel to the surface, excites only initial states of Δ_5 symmetry while E_{\perp} , i.e., the electric field component along the surface normal, excites only initial states of Δ_1 symmetry. Since $E_{\perp}/E_{||}$ will be larger for $\theta_i=45^\circ$ than for $\theta_i=15^\circ$, the peak labeled *D* in Fig. 3 can be associated with emission from initial states of Δ_1 symmetry. From Fig. 2 we can interpret peak *D* as arising from transitions between the Δ_1 initial-state band at about 2.9 eV below E_F and the final-state band of Δ_1 symmetry at about 18.3 eV above E_F , $\Delta_1(E_F-2.9 \text{ eV}) \rightarrow \Delta_1(E_F+18.3 \text{ eV})$ (see dashed arrow in Fig. 2). A variation in energy position of this

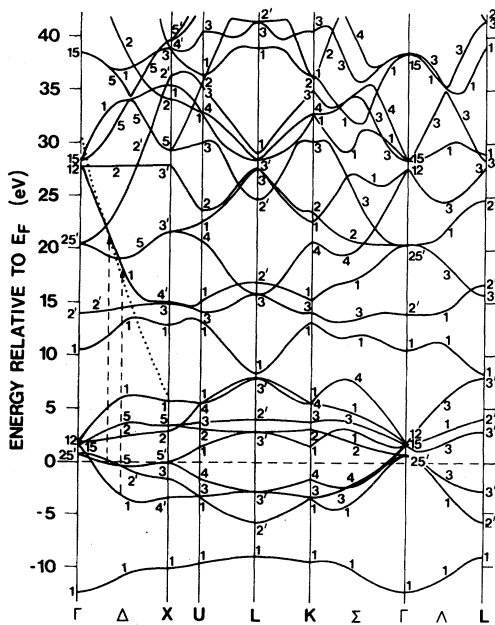


FIG. 2. Band structure of $\text{TiC}_{1.0}$ calculated using the LAPW method. A free-electron-like final-state band along the $\Gamma \rightarrow X$ symmetry line is also inserted in the figure (dotted line). Direct transitions for 21.2-eV radiation at normal emission from the (100) surface are illustrated by the dashed arrows (peaks *B* and *D* in Fig. 3).

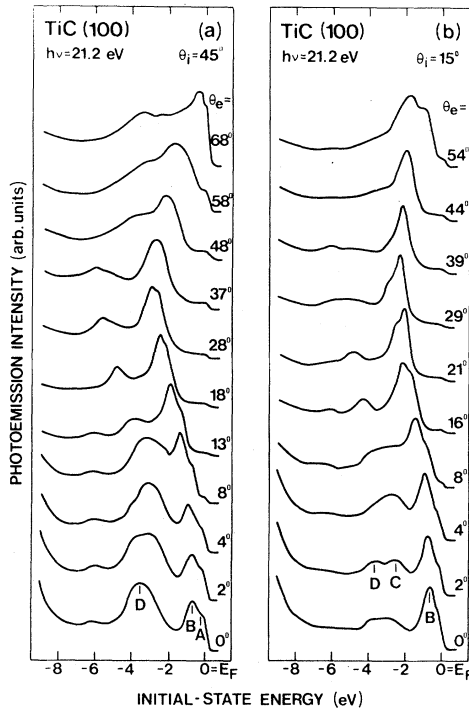


FIG. 3. Angle-resolved EDC's from TiC(100) measured at various polar angles θ_e using unpolarized He I radiation. (a) $\theta_i = 45^\circ$ and (b) $\theta_i = 15^\circ$.

peak as a function of the polar angle θ_e is clearly observed.

The peak at about -2.5 eV, labeled C in Fig. 3(b), is best resolved for $\theta_i = 15^\circ$ since peak D is much weaker in this case. To determine the origin of peak C is not so easy, however. It was earlier suggested that this structure is associated with a three-dimensional density-of-states feature.¹⁴ We would like to propose another possible explanation, namely that this peak originates from transitions between initial states of Δ_1 or Δ_2' symmetry and final states of Δ_5 symmetry, $\Delta_1(E_F - 2.4 \text{ eV}) \rightarrow \Delta_5(E_F + 18.8 \text{ eV})$ or $\Delta_2'(E_F - 1.4 \text{ eV}) \rightarrow \Delta_5(E_F + 19.8 \text{ eV})$. Both these transitions fit well with a photon energy of 21.2 eV. For normal emission both these transitions are forbidden according to the symmetry selection rules. This may explain why peak C in Fig. 3 is seen to be stronger for $\theta_e = 2^\circ$ than for $\theta_e = 0^\circ$.

A strong dispersion of the peaks near the Fermi level, labeled A and B in Fig. 3, is observed as a function of the polar angle. From the observed polarization dependence peak B can be interpreted as arising from transitions between the initial band of Δ_5 symmetry and the final band of Δ_1 symmetry, $\Delta_5(\text{near } E_F) \rightarrow \Delta_1(E_F + 21 \text{ eV})$ (see dashed arrow in Fig. 2).

Transitions from the initial band of Δ_2' symmetry to the final band of Δ_1 symmetry, $\Delta_2'(\text{near } E_F) \rightarrow \Delta_1(E_F + 22 \text{ eV})$, are believed to give rise to peak A. According to symmetry selection rules emission from the Δ_2' band is forbidden at normal electron emission, but since the energy analyzer does not have a vanishingly small acceptance angle, emission from the forbidden Δ_2' band may be observed.

The peak at about -6 eV in Fig. 3(a) is due to contamination effects. This peak disappears when the sample is better cleaned, which is shown in Fig. 3(b) where there is no sign of this peak in the normal emission spectrum. This peak grew gradually with time, and since we did not perform flash heatings in between all spectra, it only became visible in some spectra.

The energy positions of peaks A, B, C, and D are plotted versus polar angle in Fig. 4. The vertical bars on the data points indicate the estimated uncertainty of peak positions for cases where it is larger than 0.1 eV. In Fig. 4 the experimental data are compared with calculated energy positions. The dashed curves are obtained using the full calculated band structure, while the dotted curves are obtained using the free-electron-like final-state band illustrated in Fig. 2. Initial-state surfaces, on which direct transitions between bands are possible, were calculated in the repeated zone scheme of \vec{k} space. An interpolation of the calculated band structure on a denser mesh in \vec{k} space was performed in this calculation. The final-state energy and momentum is known at each point on these surfaces. By assuming conservation of k_{\parallel} (the momentum component

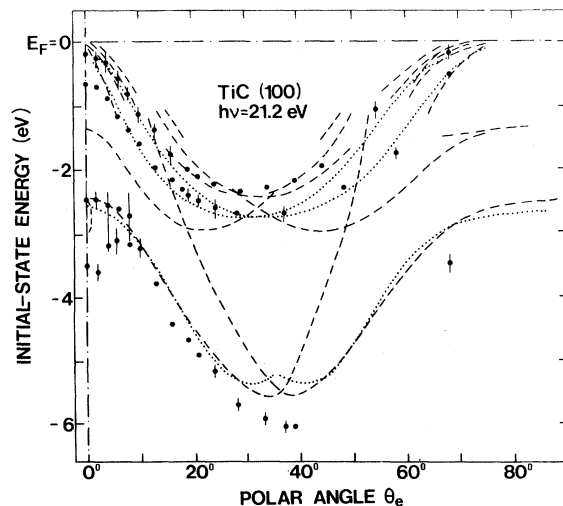


FIG. 4. Comparison between experimental and calculated peak positions as functions of polar angles along the $\langle 011 \rangle$ azimuth. See text for details.

parallel to the surface) during propagation through the surface, the detection angle for electrons which have undergone direct transitions becomes

$$\theta_e = \arcsin \frac{\hbar |k_{||}|}{|2m(E_i - E_F + \hbar\nu - \phi)|^{1/2}},$$

where $E_i - E_F$ represents the initial-state energy, relative to the Fermi level, and ϕ is the work function. For the calculated curves in Fig. 4 a work-function value of 4.0 eV (Ref. 32) has been used. Both primary-cone emission and secondary-cone emission, involving G_{TTT} and G_{TTT} reciprocal-lattice vectors, have been accounted for in the calculation. The comparison between the experimental results and the calculated curves shows that the trends in the experimental polar-angle dependence of peak positions agree quite well with the trends of the calculated curves. Peak *B* is seen to lie about 0.5 eV deeper below E_F than the calculated position at $\theta_e = 0^\circ$, but the angle dependence agrees well with the calculated dependence. Also for peak *A* there is a good agreement between experimental and calculated curves.

When concentrating on the dashed curves (full calculated band structure) an obvious difference between experimental and calculated results occurs for peak *D* when $\theta_e < 10^\circ$. This difference, we believe, is partly due to the interpolation scheme used in the program to calculate these curves. The interpolation between the calculated band-structure points into a denser mesh of \mathbf{k} space becomes less accurate when bands cross each other. In this case it is the crossing between the final-state bands Δ_1 and the doubly degenerate Δ_5 , at about 19 eV above E_F (see Fig. 2), that causes the problem. Only a small change in the photon energy was found to give rise to significant changes in the calculated polar-angle dependence for $\theta_e < 10^\circ$. If the photon energy is increased a few tenths of an eV the dashed curve will move downwards, in Fig. 4, so it better fits the experimental points of peak *D*.

For peak *C* there are two alternatives. If the peak is associated with transitions $\Delta'_2(E_F - 1.4 \text{ eV}) \rightarrow \Delta_5(E_F + 19.8 \text{ eV})$, the calculated band lies about 1 eV closer to E_F than the experimental points do. If the peak is instead associated with transitions $\Delta_1(E_F - 2.4 \text{ eV}) \rightarrow \Delta_5(E_F + 18.8 \text{ eV})$, the experimental points at normal emission lie pretty close to the calculated band. The rather strange appearance of this calculated band, the short dashed curve going from -2.5 to -2.9 eV in Fig. 4, is due to the same interpolation problem as discussed above.

In Figs. 5, EDC's from the TiC(100) surface, recorded at different polar angles along the $\langle 011 \rangle$ azimuth, using unpolarized NeI radiation, are shown. The incidence angle θ_i is 45° for the spectra

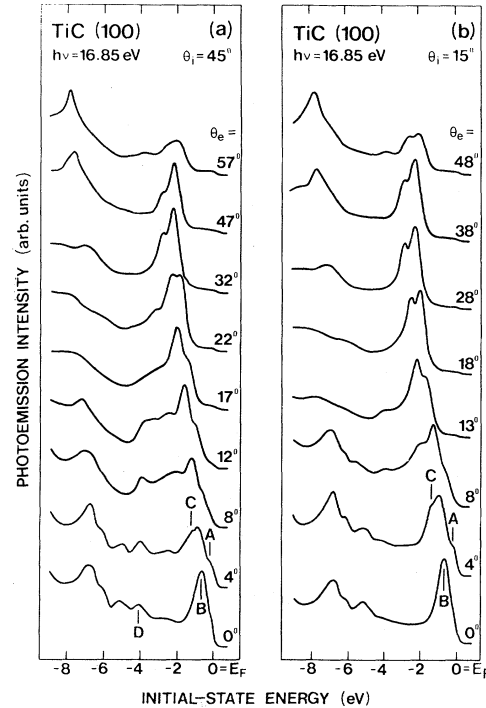


FIG. 5. Angle-resolved EDC's from TiC(100) measured at various polar angles θ_e using unpolarized NeI radiation. (a) $\theta_i = 45^\circ$ and (b) $\theta_i = 15^\circ$.

shown in Fig. 5(a) and 15° for those shown in Fig. 5(b). The peaks labeled *B*, *C*, and *D* in Figs. 5 are due to direct transitions. Peak *B* corresponds to transitions between the Δ_5 initial-state band at about 0.4 eV below E_F and the final-state band of Δ_1 symmetry at about 16.4 eV above E_F , $\Delta_5(E_F - 0.4 \text{ eV}) \rightarrow \Delta_1(E_F + 16.4 \text{ eV})$. Peaks *C* and *D* are interpreted as associated with transitions $\Delta'_2(E_F - 0.9 \text{ eV}) \rightarrow \Delta_1(E_F + 15.9 \text{ eV})$ and $\Delta_1(E_F - 3.7 \text{ eV}) \rightarrow \Delta_1(E_F + 13.1 \text{ eV})$, respectively. For peak *D* a strong polarization effect is observed when comparing the spectra shown in Figs. 5(a) and 5(b), which again unambiguously identify the symmetry of the initial-state band to be Δ_1 .

The energy positions of peaks *B*, *C*, and *D* are plotted versus polar angles in Fig. 6. The solid dots indicate the dispersion of the peaks *B*, *C*, and *D* and the unfilled dots indicate the weak shoulder labeled *A* in Figs. 5. Also shown in Fig. 6 are the calculated curves, where the dashed and dotted curves represent results obtained using the full calculated band structure and the free-electron-like final-state band, respectively. Also at this photon energy the trends in the experimental polar-angle dependence of peak positions agree well with the trends of the cal-

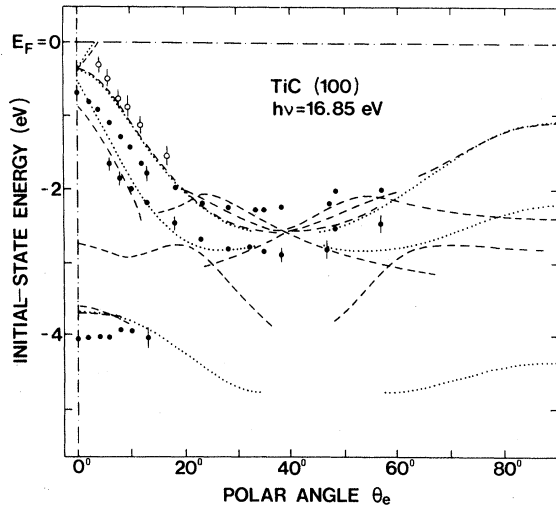


FIG. 6. Comparison between experimental and calculated peak positions as functions of polar angles along the $\langle 011 \rangle$ azimuth. See text for details.

culated curves. For small θ_e , however, the peaks *B* and *D* lie about 0.3 eV deeper below E_F than the calculated positions.

The features between 5 and 8 eV binding energy, in Figs. 5, are plotted versus kinetic energy in Fig. 7.

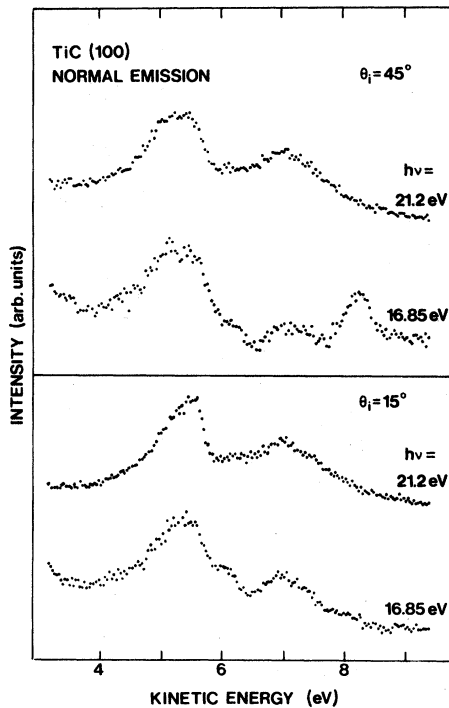


FIG. 7. Normal emission spectra for TiC(100) measured at photon energies of 16.85 and 21.2 eV for $\theta_i = 45^\circ$ and 15° .

Also shown in Fig. 7 are spectra recorded with a photon energy of 21.2 eV. The EDC's obtained show that the two major features, around 5.6 and 7 eV kinetic energy, remain at fixed kinetic energies as the photon energy changes from 16.85 to 21.2 eV. We therefore identify them with emission of secondary electrons.¹⁴ These secondary electrons have been excited to final states of higher energy and then scattered inelastically and cascaded to a lower final state before emission into vacuum. The two peaks around 7 and 5.6 eV kinetic energy are associated with emission from $X_1(E_F + 12.5$ eV) and $\Gamma_1(E_F + 10.5$ eV) into vacuum, respectively.

C. The (110) surface

In Fig. 8 EDC's from TiC(110) at photon energies of 16.85 and 21.2 eV are shown. The EDC's are recorded at two different incidence angles, $\theta_i = 15^\circ$ and 45° . Also shown in Fig. 8 is the calculated band

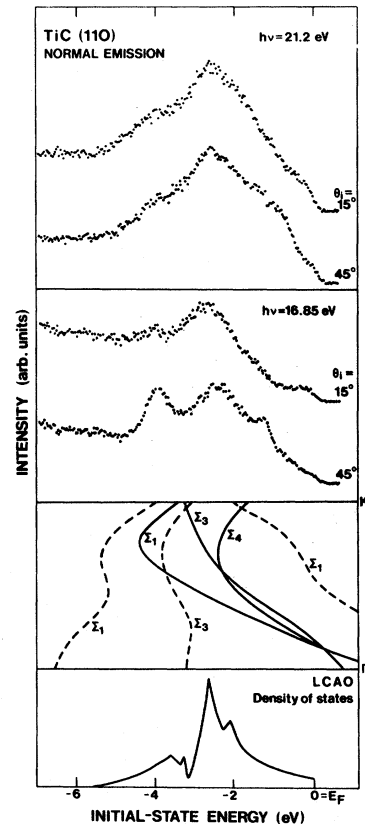


FIG. 8. Normal emission EDC's from TiC(110) measured at photon energies of 21.2 and 16.85 eV for $\theta_i = 15^\circ$ and 45° are shown in the upper half of the figure. The lower half shows the calculated band structure for TiC(110) along the $\Gamma \rightarrow K$ symmetry line and a LCAO density-of-states calculation. See text for further details.

structure of $\text{TiC}_{1.0}$ along the $\Gamma \rightarrow K$ symmetry line. The solid lines represent the initial-state bands and the dashed lines represent the final-state bands displaced downwards by 16.85 eV. At the bottom of Fig. 8 a linear combination of atomic orbitals (LCAO) density-of-states calculation by Neckel *et al.*²⁸ is shown.

At a photon energy of 16.85 eV a strong polarization effect is observed for the peak at about -4 eV initial-state energy. According to the symmetry selection rules,³¹ this polarization effect identifies this peak as due to emission from an initial-state band of Σ_1 symmetry. This peak can be interpreted from Fig. 8 as due to transitions between the Σ_1 initial-state band at about 4 eV below E_F and the Σ_1 final-state band, shown as a dashed line in Fig. 8, if the final-state band is moved upwards in energy about 0.5 eV. The peak should not arise from transitions to the Σ_3 final-state band since such transitions ($\Sigma_1 \rightarrow \Sigma_3$) are forbidden in normal emission. The peak discussed above is not observed for a photon energy of 21.2 eV because then there exists no proper final-state band.

Both for 16.85 and for 21.2 eV there is a peak at about -2.7 eV, which we cannot identify as due to direct transitions. This peak we believe is due to three-dimensional density-of-states (DOS) effects, since there are flat bands extending through major portions of the Brillouin zone at this energy; see Fig. 2. The LCAO density-of-states calculation, see Fig. 8, also has a maximum at this energy.

D. The (111) surface

Angle-resolved EDC's for $\text{TiC}(111)$ recorded at a photon energy of 21.2 eV are shown in Fig. 9. The incidence angle is $\theta_i = 45^\circ$ and the polar angles θ_e along the $\langle 211 \rangle$ azimuth are as indicated. A polar-angle dependence is observed for the peak at an initial-state energy of -4.4 eV. This peak is detected at polar angles between 22° and 29° and also weakly at polar angles greater than 53° , and could be reflecting emission from the flat region of the Σ_1 initial-state band along the $\Gamma \rightarrow K$ symmetry line, since the angle between the (111) and (110) planes in the above described azimuthal orientation corresponds to a polar angle of 35° . There is also a structure observed at about 4-eV binding energy in the spectra from the (110) surface which supports this.

Intensity changes with polar angle are observed for the peak at about -2.8 eV. This peak, however, shows no dispersion and since the LCAO density-of-state calculations, see Fig. 8, have a maximum at this energy, it can be explained as being due to either one- or three-dimensional density-of-state effects as proposed earlier.¹⁴ In the case of one-dimensional

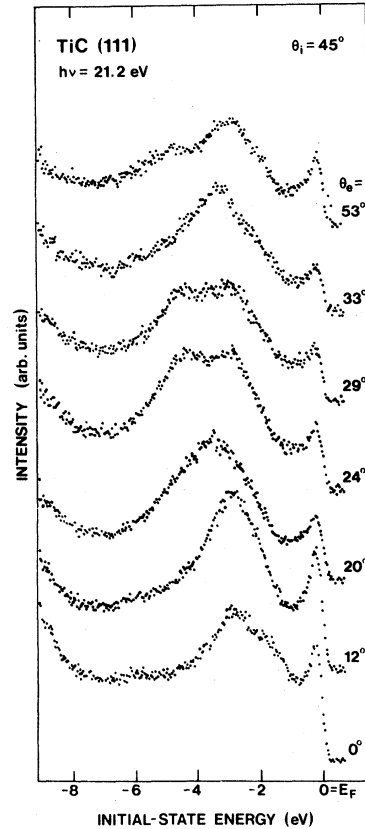


FIG. 9. Angle-resolved EDC's from $\text{TiC}(111)$ measured at various polar angles θ_e using unpolarized He I radiation.

DOS effects the peak can be reflecting emission from the band near the L'_3 point. It cannot, however, be described by direct transitions from the L'_3 point, since there are no final-state bands available at this energy. It can also be associated with transitions between the Λ_1 initial-state band at about 2.8 eV below E_F and the final-state band of Λ_3 symmetry at about 18.8 eV above E_F , $\Lambda_1(E_F - 2.8 \text{ eV}) \rightarrow \Lambda_3(E_F + 18.3 \text{ eV})$. The peak near the Fermi level is the only peak that shows a polarization dependence and this peak originates from a surface-induced state, as reported earlier.¹²

E. Comparison

In comparing the experimental results obtained for the three TiC surfaces studied, an obvious difference in the applicability of the direct transition model is noticed. While our results for the $\text{TiC}(100)$ surface indicate that most of the structures observed in the photoemission spectra can be explained in terms of direct transitions, this is not the case for the (110) and (111) surfaces. For the (110) surface

there are some structures that can be associated by direct transitions, but density-of-state features are also observed in these spectra. For the (111) surface there are no structures observed that unambiguously can be interpreted as being due to direct transitions. In this latter case the results are thus interpreted in terms of density-of-state effects. Three-dimensional density-of-states features were observed in a previous ARPES investigation¹⁴ of the (100) and (111) surfaces of a $\text{TiC}_{0.93}$ crystal and were attributed to either the effects of bulk vacancies in the crystal or to surface inhomogeneities incurred in the cleaning process. Our results for the (100) surface, however, indicate that the bulk vacancies in a $\text{TiC}_{0.93}$ crystal do not give rise to dominant three-dimensional density-of-states effects since most of our data could be explained in terms of direct transitions. Surface inhomogeneities incurred in the preparation process may explain why three-dimensional density-of-states effects make a dominant contribution in the photoemission spectrum from the (111) surface since the cleaning process in this case involved sputtering and annealing. For the (110) surface, on the other hand, the cleaning process consisted of flash heatings, as for the (100) surface. Thus surface inhomogeneities incurred in the preparation process do not seem likely to explain dominant three-dimensional density-of-states features in the spectra of the (110) surface. We propose that the major reason for observing dominant three-dimensional density-of-states features in the photoemission spectra from the (110) and (111) surfaces is a lack of appropriate final-state bands in these directions for the photon energies used. This can be seen in Fig. 2. For the (100) surface an appropriate final-state band of Δ_1 symmetry with a nearly free-electron character is available at the photon energies used, as seen in Fig. 2. This was also the case for $\text{TiN}(100)$ and seems to hold also for other nitrides and carbides. Thus the (100) surface seems to be a fortunate case for doing ARPES investigations on nitride and carbide surfaces.

We believe that the major reason why the individual bands and their dispersions could not be unambiguously identified and mapped out in the previous investigation of the $\text{TiC}(100)$ surface was due to the lack of a calculated band structure at high enough final-state energies. The photoemission results from the (111) surface may be affected by the different cleaning procedure used for this particular surface, but we suggest that the major reason for the

three-dimensional density-of-states effects observed is due to the lack of appropriate final-state bands.

IV. SUMMARY

The band structure of nonstoichiometric $\text{TiC}_{0.93}$ has been studied by utilizing angle-resolved photoemission and the results are interpreted using the bulk band structure, which was calculated for stoichiometric $\text{TiC}_{1.0}$ using the LAPW method. Experiments were carried out on the (100), (110), and (111) surfaces of the TiC crystal.

For the $\text{TiC}(100)$ surface strong polarization and polar-angle dependencies were observed in the photoemission spectra. This allowed direct identification of individual bands, and their energy locations and dispersions were mapped out by applying the direct-transition model. A good agreement between the experimental and calculated band-structure results was obtained. Direct transitions were thus shown to make the dominant contribution to the photoemission spectrum of the $\text{TiC}(100)$ surface. The same conclusion was obtained in an earlier study of the $\text{TiN}(100)$ surface.¹⁵

The results from the (110) and (111) surfaces could not be interpreted in such a straightforward manner. For these surfaces three-dimensional density-of-states effects were found to make a dominant contribution, which we attribute to a lack of appropriate final-state bands in these directions for the photon energies used. The fact that the vacancies in the $\text{TiC}_{0.93}$ crystal would cause such an effect is ruled out by our results on the (100) surface.

The applicability of the direct-transition model shown for $\text{TiC}(100)$ in the present investigation and for $\text{TiN}(100)$ in our earlier report seem to indicate that the (100) surfaces of nitrides and carbides are especially well suited for band mapping when using angle-resolved photoemission and excitation radiation from conventional resonance lamps. Our preliminary results on $\text{ZrN}(100)$ and $\text{VN}(100)$ also indicate this.

ACKNOWLEDGMENTS

Financial support from the Swedish Natural Research Council for carrying out this research is acknowledged by A.C. and L.I.J. The band-structure computations were performed at Interfakultäres Rechenzentrum der Technischen Universität, Wien.

- ¹L. Ramqvist, K. Hamrin, G. Johansson, A. Fahlman, and C. Nordling, *J. Phys. Chem. Solids* **30**, 1835 (1969); **31**, 2669 (1970).
- ²D. W. Fischer, *J. Appl. Phys.* **41**, 3922 (1970).
- ³H. Ihara, Y. Kumashiro, and A. Itoh, *Phys. Rev. B* **12**, 5465 (1975); **14**, 1707 (1976).
- ⁴J. F. Alward, C. Y. Fong, M. El-Batanouny, and F. Wooten, *Phys. Rev. B* **12**, 1105 (1975); *Solid State Commun.* **17**, 1063 (1975).
- ⁵V. A. Gubanov and E. Z. Kurmaev, *Int. J. Quantum Chem.* **9**, 297 (1975).
- ⁶K. Schwarz, A. Neckel, and A. M. Bradshaw, *Chem. Phys. Lett.* **41**, 311 (1976).
- ⁷S. Manninen and T. Paakkari, *J. Phys. C* **9**, 95 (1976).
- ⁸L. I. Johansson, A. L. Hagström, B. E. Jacobson, and S. B. M. Hagström, *J. Electron Spectrosc. Relat. Phenom.* **10**, 259 (1977).
- ⁹A. L. Hagström, L. I. Johansson, S. B. M. Hagström, and A. N. Christensen, *J. Electron Spectrosc. Relat. Phenom.* **11**, 75 (1977).
- ¹⁰L. I. Johansson, P. M. Stefan, M. L. Shek, and A. N. Christensen, *Phys. Rev. B* **22**, 1032 (1980).
- ¹¹J. H. Weaver and F. A. Schmidt, *Phys. Lett.* **77A**, 73 (1980).
- ¹²A. M. Bradshaw, J. F. van der Veen, F. J. Himpsel, and D. E. Eastman, *Solid State Commun.* **37**, 37 (1980).
- ¹³L. I. Johansson, P. M. Stefan, M. L. Shek, and A. N. Christensen, *Solid State Commun.* **36**, 965 (1980).
- ¹⁴J. H. Weaver, A. M. Bradshaw, J. F. van der Veen, F. J. Himpsel, D. E. Eastman, and C. Politis, *Phys. Rev. B* **22**, 4921 (1980).
- ¹⁵L. I. Johansson, A. Callenäs, P. M. Stefan, A. N. Christensen, and K. Schwarz, *Phys. Rev. B* **24**, 1883 (1981).
- ¹⁶W. K. Schubert, R. N. Shelton, and E. L. Wolf, *Phys. Rev. B* **23**, 5097 (1981).
- ¹⁷W. K. Schubert, R. N. Schelton, and E. L. Wolf, *Phys. Rev. B* **24**, 6278 (1981).
- ¹⁸H. Höchst, R. D. Bringans, P. Steiner, and Th. Wolf, *Phys. Rev. B* **25**, 7183 (1982).
- ¹⁹A. N. Christensen, *J. Cryst. Growth* **33**, 99 (1976).
- ²⁰J.-E. Sundgren, B.-O. Johansson, and S.-E. Karlsson, *Appl. Phys.* (in press).
- ²¹L. Hedin and S. Lundquist, in *Solid State Physics*, edited by H. Ehrenreich, F. Seitz, and D. Turnbull (McGraw-Hill, New York, 1969), Vol. 23, pp. 1-181.
- ²²P. Hohenberg and W. Kohn, *Phys. Rev.* **135**, B864 (1964); W. Kohn and L.-J. Sham, *ibid.* **140**, A1133 (1965).
- ²³J. F. Janak, *Phys. Rev. B* **18**, 7165 (1978).
- ²⁴K. Schwarz, *Phys. Rev. B* **5**, 2466 (1972).
- ²⁵L. Hedin, and S. Lundquist, *J. Phys. (Paris) Colloq.* **33**, C3-73 (1972); U. von Barth and L. Hedin, *J. Phys. C* **5**, 1629 (1972); O. Gunnarsson and B. I. Lundquist, *Phys. Rev. B* **13**, 4274 (1976).
- ²⁶G. P. Kerker, *Phys. Rev. B* **24**, 3468 (1981); G. Borstel and M. Neumann, *ibid.* **23**, 3113 (1981).
- ²⁷L. C. Davis and L. A. Feldkamp, *Solid State Commun.* **24**, 141 (1980).
- ²⁸A. Neckel, P. Rastl, R. Eibler, P. Weinberger, and K. Schwarz, *J. Phys. C* **9**, 579 (1976).
- ²⁹O. K. Andersen, *Phys. Rev. B* **12**, 3060 (1975); D. D. Koelling and G. O. Arbman, *J. Phys. F* **5**, 2041 (1975).
- ³⁰A. Neckel, *Int. J. Quantum Chem.* (in press).
- ³¹J. Hermanson, *Solid State Commun.* **22**, 9 (1977).
- ³²C. Oshima, T. Tanaka, M. Aono, R. Nishitani, S. Kawai, and F. Yajima, *Appl. Phys. Lett.* **35**, 822 (1979).